Radiative effects of increased water vapor in the upper Saharan air layer associated with enhanced dustiness

Ryder, C. L. ORCID: https://orcid.org/0000-0002-9892-6113 (2021) Radiative effects of increased water vapor in the upper Saharan air layer associated with enhanced dustiness. Journal of Geophysical Research: Atmospheres, 126 (21). e2021JD034696. ISSN 2169-8996 doi: https://doi.org/10.1029/2021JD034696 Available at https://centaur.reading.ac.uk/100761/

JGR Atmospheres

RESEARCH ARTICLE
10.1029/2021JD034696

Key Points:

- Observations show enhanced moisture in the upper Saharan Air Layer (SAL) associated with dust, counter to the conventional dry layer model
- Enhanced moisture reduces the magnitude of the negative direct radiative effect from dust at the top-of-atmosphere by 17%
- Observed water vapor structure leads to enhanced cooling in the moist upper-SAL and heating in the dry lower-SAL under dustier conditions

Supporting Information:

Supporting Information may be found in the online version of this article.

Correspondence to:

C. L. Ryder,
c.l.ryder@reading.ac.uk

Citation:

Ryder, C. L. (2021). Radiative effects of increased water vapor in the upper Saharan Air Layer associated with enhanced dustiness. *Journal of Geophysical Research: Atmospheres*, *126*, e2021JD034696. https://doi.org/10.1029/2021JD034696

Received 1 FEB 2021
Accepted 10 OCT 2021

Radiative Effects of Increased Water Vapor in the Upper Saharan Air Layer Associated With Enhanced Dustiness

C. L. Ryder[1]

[1]Department of Meteorology, University of Reading, Reading, UK

Abstract The Saharan Air Layer (SAL) is known as an elevated, well-mixed, warm, dry, frequently dusty layer and plays an important role in regional climate and dust transport. A new analysis of aircraft observations of haboob-driven dust events shows that although increased dustiness in the SAL is associated with drier conditions in the lower-SAL as expected, dustiness is also associated with increased moisture in the upper-SAL, likely originating from cold pool outflows driving the dust uplift. We assess the radiative effects of the observed dust and increased water vapor (WV). The observed WV in the upper-SAL affects the top-of-atmosphere (TOA) direct radiative effect (DRE), while lower-SAL WV affects the surface DRE and column atmospheric heating. TOA DRE is negative for dust only, while including both the observed dust and WV reduces the magnitude of the negative TOA DRE by 17% (3.0 ± 0.8 Wm^{-2}) when AOD > 0.6. The observed WV structure increases the magnitude of the negative surface DRE from dust by 8% (5.1 ± 0.8 Wm^{-2}) and increases atmospheric heating by 17% (8.0 ± 0.6 Wm^{-2}). These effects are driven by longwave (LW) radiation, whereby WV changes increase the positive TOA LW DRE, decrease the surface LW DRE and change the sign of LW atmospheric heating from negative to positive. WV leads to enhanced cooling in the moist upper-SAL and heating in the dry lower-SAL under dustier conditions. Increased WV in the SAL is consistent with other studies demonstrating increasing Saharan WV. This study demonstrates the importance of upper-SAL WV in determining the radiative effect of dust.

Plain Language Summary During summer, warm, dry, and dusty air are transported from the Sahara across the Atlantic Ocean in an elevated plume. This plume has many impacts on climate, such as suppressing convection which may be important to hurricane development, and transporting dust particles that can supply nutrients to the oceans and degrade respiratory health. Previously the plume has been found to be very dry, but new observations from a research aircraft show that high levels of moisture are found at its top. This is important because it alters the balance of heating and cooling at different altitudes within the atmosphere, and may impact how Saharan air interacts with the weather in the Atlantic region. We find that the addition of moisture at the top of the plume adds a warming of 17% compared to the effects from dusty air. We show that the likely cause of the enhanced moisture comes from the method of dust uplift: cold pool outflows from deep convection (haboobs). Therefore future study should take into account the vertical distribution of moisture in Saharan dust plumes as well as the dust itself, as well as exploring the role of haboobs in Saharan meteorology.

1. Introduction

The Saharan Air Layer (SAL) is conventionally considered to be a deep warm, dry, elevated layer of air that exists over the tropical North Atlantic Ocean from late spring to early fall, frequently containing mineral dust transported from North Africa (Braun, 2010). The SAL originates from strong surface heating over the Sahara desert, where a deep, well-mixed, warm, dry boundary layer develops, typically extending up to 5–6 km, known as the Saharan Boundary Layer (Engelstaedter et al., 2015; Marsham et al., 2013). The SAL, and any embedded mineral dust, is transported westwards by prevailing winds and steered by African Easterly Waves. As it moves over the Atlantic Ocean, it is undercut by a moist marine boundary layer (MBL), forming an elevated mixed layer known as the SAL, characterized by near-constant potential temperatures and water vapor (WV) mixing ratios, and retaining its structure as it is transported westwards (Carlson, 2016; Dunion & Velden, 2004).

In the original conceptual model of the SAL (e.g., Carlson & Prospero, 1972; Dunion, 2011; Karyampudi et al., 1999; Prospero & Carlson, 1972), the SAL is shown to be warm, dry, and to varying degrees, dust laden.

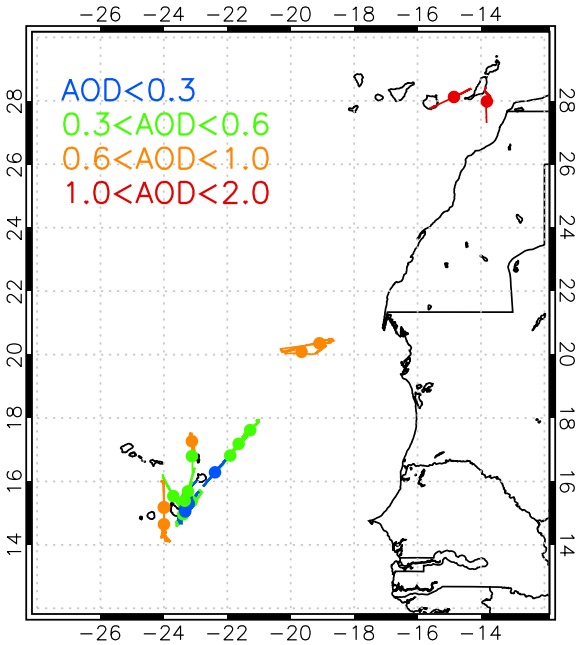

Figure 1. Locations of AER-D aircraft profiles analyzed in this study. Lines show locations sampled during profile ascents or descents, solid dots indicate mean profile location. Colors indicate AOD as shown in the legend.

For example, reported values of WV mixing ratios within the eastern SAL are around 2–5 g/kg (Carlson & Benjamin, 1980; Carlson & Prospero, 1972; Ismail et al., 2010; Karyampudi et al., 1999), and 1–6 g/kg in the western SAL (Dunion, 2011; Dunion & Velden, 2004). Kanitz et al. (2014) present measurements across the width of the tropical Atlantic, finding WV mixing ratios between 3 and 7 g/kg within the SAL. Warm, dry anomalies in the SAL between 800 and 900 hPa have been shown to be related to increased dust optical depth. Together the dusty, dry anomalies are responsible for heating the lower SAL and maintaining the temperature inversion its base, as well has playing a role in suppressing deep convection and increasing low cloud fraction (Doherty & Evan, 2014; Wong & Dessler, 2005; Wong et al., 2009).

Around 50% of dust events in the summertime Sahara are driven by cold pool outflows (haboobs; Marsham & Ryder, 2021), with the dust being associated with elevated moisture levels deriving from moist downdrafts (Marsham et al., 2008, 2013). Several studies have described the role of cold pool outflows and density currents in transporting dust and moisture into the arid Sahara (Allen et al., 2013; Engelstaedter et al., 2015; Flamant et al., 2007). Marsham et al. (2016) examined the relative radiative effects of dust and WV in the Saharan heat low (SHL), finding that WV variations exert a dominant role on the top-of-atmosphere (TOA) radiation budget, while dust variability was dominant in driving atmospheric heating and surface radiation. Gutleben et al. (2019) found that SAL WV mixing ratios over the western Atlantic for one dust event were elevated compared to those in the surrounding free atmosphere, and found that the altered WV profile within the dust led to substantial changes in radiative heating rates.

Here, we examine dust and WV aircraft observations in the tropical east Atlantic Ocean region. During research flights, it was noticed that specific humidity often increased when dust layers were penetrated, and was particularly noticeable during a few extremely large dust events (Marenco et al., 2018). Since this increased moisture within the dusty SAL is counter to the conventional model of a dry, dusty SAL, here we examine the evidence from airborne observations and evaluate the radiative effect of the observed changes in dust and enhanced WV.

2. Methods

2.1. Aircraft Observations

We present meteorological and aerosol in-situ aircraft observations from the AERosol Properties-Dust (AER-D) airborne field campaign (Marenco et al., 2018) which took place during August 2015 in the region of the Cape Verde Islands (Figure 1). The Facility for Atmospheric Airborne Measurements BAe146 research aircraft sampled a series of dust events in the SAL between August 7 and 25, 2015, described in more detail by Ryder et al. (2018), Liu et al. (2018), Marenco et al. (2018), where microphysical, chemical, optical, and radiative properties of the dust samples are presented.

Here, we use in-situ observations from 22 aircraft profile descents and ascents as shown in Figure 1, sampled during 6 flights (also shown in Ryder et al., 2018, their Table 2). Profiles cover altitudes from close to the ocean surface to above the SAL, generally ∼5.5 km. All the dust events sampled during AER-D were initially driven by outflows from mesoscale convective systems ("haboobs," identified in Ryder et al., 2018), which had been mixed vertically throughout the Saharan boundary layer by convective mixing before being advected over the ocean in an elevated SAL. We exclude one unusual, intense dust event where the dust sampled was much closer to the surface, because the unusual vertical dust and WV structure lead to very different radiative effects. This particular event is examined by Marenco et al. (2018) in more detail.

Airborne measurements of temperature are taken from a Rosemount/Goodrich type 102 Total Air Temperature probe, using the non-deiced models for all flights except b934 when data is not available, and when the deiced model was used instead. Dew point temperature measurements used to calculate WV mixing ratios are taken from the Sky Phys Tech Inc. Nevzorov total water content probe (Korolev et al., 1998), except for flights b923, b934, and b932 Profile 1 where they are taken from the General Eastern 1011B chilled mirror hygrometer. Pressure was measured by a reduced vertical separation minimum data system.

Ryder et al. (2018) have shown that the aerosol load sampled was predominantly mineral dust, including the aerosol in the marine boundary layer. Here, we take a straightforward indication of dust loading from the dust extinction at 550 nm, calculated by summing dust scattering and absorption. Scattering is measured by a TSI 3563 integrating nephelometer (550 nm wavelength used here) and absorption measurements were made by a Radiance Research particle soot absorption photometer (PSAP) at 567 nm. All extinction is assumed to be due to dust aerosol, as this was shown to be the dominant aerosol type in filter sample analysis, even within the MBL (Ryder et al., 2018). Additionally, the scattering angstrom exponent (450–700 nm) measured by the nephelometer was nearly always negative indicating the dominance of coarser dust particles (D. T. Liu et al., 2018), aircraft lidar depolarization indicated dust, and dust sampled was clearly visible in satellite imagery originating from the Sahara. Further details and processing information can be found in Ryder et al. (2018). Extinction is integrated vertically from aircraft profiles to provide AODs at 550 nm.

2.2. Radiative Transfer Calculations

We employ the Suite Of Community RAdiative Transfer codes based on Edwards and Slingo (SOCRATES; Edwards & Slingo, 1996; Manners et al., 2017) radiative transfer model (RTM) in order to calculate radiative fluxes. SOCRATES is the RTM implemented by the family of UK Met Office numerical weather prediction and climate models. Here, we use the spectral setup analogous to that from HadGEM3 model Global Atmosphere 6 configuration (Walters et al., 2011). A two stream practical improved flux method is used (Zdunkowski et al., 1980).

Shortwave (SW) fluxes are calculated over six spectral bands from 0.2 to 10 μm and longwave (LW) fluxes are calculated in nine spectral bands from 3.3 to 100 μm. Gaseous absorption is represented according to Cusack et al. (1999) using a correlated-k method. WV terms are based on the HITRAN 2001 database (Rothman et al., 2003) for gaseous absorption coefficients, with updates up to 2003. The WV continuum is represented using version 2.4 of the CKD model. TOA incoming solar radiation is set to 1,365 Wm^{-2}.

SOCRATES requires aerosol vertical profiles in terms of mass mixing ratios. These are calculated to represent dust from the measured in-situ aerosol extinction profiles, converted to a mass loading by using a field campaign specific mass extinction coefficient of 0.36 m^2g^{-1} (Ryder et al., 2018). This value represents the full size distribution up to 100 μm diameter.

We use 122 vertical levels in SOCRATES, covering 1007 to 0.0005 hPa, with resolution ∼20 hPa in the lower atmosphere, including the SAL. Observations of dust mass mixing ratio, WV mixing ratio, and temperature are regridded to the required vertical grid. Only dust aerosols are included. At altitudes above where aircraft data were measured, dust concentrations are set to zero, and temperature and WV values are set to revert to values from a tropical standard profile (Anderson et al., 1986). Ozone, methane, carbon monoxide, carbon dioxide, nitrous oxide, and oxygen profiles are taken from Randles et al. (2012). SW surface albedo is set to 0.05 representative of an ocean surface and LW surface emissivity to 0.982 in all spectral intervals.

Dust optical properties are calculated spectrally in the LW and SW spectra using lognormal size distribution parameters representing the AER-D SAL average, as given in Ryder et al. (2018). In the SW, complex refractive index data are taken from Colarco et al. (2014) and LW values from Volz (1973) since these data sets fall centrally in the range from literature (Ryder et al., 2019) and cover the full spectral range required. Mie scattering code (and therefore a spherical particle assumption) is used to calculate spectral optical properties of mass extinction coefficient, single scattering albedo (SSA), and asymmetry parameter, which are applied in SOCRATES and are shown in Table 1. The SSA at visible wavelengths is 0.86, considerably lower than the AER-D campaign mean value of 0.95 at 550 nm (Ryder et al., 2018). The difference occurs due to the spectral averaging applied here which incorporates absorption increasing significantly toward smaller solar wavelengths, as well as the use of the Colarco et al. (2014) imaginary refractive index of 0.0024 at 550 nm

Table 1
Optical Properties Applied in SOCRATES for Each Spectral Band Estimated Using Refractive Index Data From Colarco et al. (2014) for the SW, Volz (1973) for the LW, and the AER-D Mean Size Distribution (Ryder et al., 2018)

Spectral range	Lower wavelength, μm	Upper wavelength, μm	MEC/ m^2g^{-1}	SSA	Asymmetry parameter
SW	0.20	0.32	0.36	0.70	0.83
	0.32	0.69	0.36	0.86	0.76
	0.69	1.19	0.36	0.95	0.71
	1.19	2.38	0.35	0.93	0.69
	2.38	10.00	0.26	0.82	0.71
LW	25.0	10,000.0	0.05	0.28	0.29
	18.2	25.0	0.15	0.36	0.32
	12.5	18.2	0.13	0.42	0.52
	13.3	16.9	0.10	0.37	0.54
	8.3	12.5	0.17	0.42	0.56
	8.9	10.1	0.28	0.45	0.46
	7.5	8.3	0.09	0.41	0.74
	6.7	7.5	0.16	0.62	0.72
	3.3	6.7	0.24	0.87	0.68

compared to a value of 0.0010 derived in Ryder et al. (2018). SOCRATES includes both absorption and scattering in the LW spectrum.

Sensitivity tests have also been carried out using more and less absorbing dust at solar wavelengths, typical of the range of values applied in different climate models (rather than the uncertainty in the observations themselves). These were calculated using the more absorbing OPAC data set refractive indices with the OPAC transported mineral dust size distribution (Hess et al., 1998), and the less absorbing refractive index data set of Balkanski et al. (2007) combined with a smaller dust size distribution (Dubovik et al., 2002). At infrared wavelengths, sensitivity to dust is tested by varying the dust size distribution to the smaller one of Dubovik et al. (2002) and the refractive index to that from OPAC. These calculations yield SSA values of 0.74 and 0.94 for the more and less absorbing cases respectively for the spectral band spanning wavelengths of 0.32–0.69 μm. These sensitivity tests are used to provide uncertainties for DRE calculations in Section 3.

Surface temperatures for the LW calculations are set based on values observed from aircraft in-situ observations or dropsondes. SW diurnal averages are calculated by running SOCRATES at three solar zenith angles based on the location and time of year of observations, which are multiplied by a Gaussian weight and summed.

For each of 22 profiles, four radiative transfer simulations are conducted, as outlined in Table 2, to isolate the effects of the altered WV profile in the SAL, the presence of dust, and their combined effect. The temperature profile is taken from aircraft measurements in all experiments. For the CONTROL, no radiative effects of dust are included. To create a WV profile representative of background conditions for the region for the control, a smoothed median of the aircraft WV profiles where AOD is less than 0.3 is taken (blue lines in Figures 1e and 2a), which represents a non-SAL background WV profile. Smoothing is used to highlight the differences between the CONTROL and other experiments. We do not use the tropical standard WV profile (Anderson et al., 1986), because the non-SAL atmosphere in the region is significantly moister than this (see Figure 1e). The three perturbation experiments shown in Table 2 allow the quantification of the radiative impacts relative to a typical background, non-dusty state in the region. For the dust only experiment (DU), dust observations from aircraft measurements are included, but the background WV profile maintained, such that only the radiative impact of dust is assessed. For the WV only experiment, no dust is included, but the WV profile used is taken from the aircraft observations, to explicitly determine the radiative effect of the changing WV profile. Finally, for DU + WV, both the aircraft-observed dust and WV profiles are included to assess their combined effect. For each experiment, vertical profiles of SW and LW radiative fluxes and heating rates are calculated for all aircraft profiles.

Table 2
SOCRATES Experiments. Each Experiment Is Performed for Each of 24 Aircraft Profiles

Experiment name	Abbreviation	Temperature profile	Dust profile	Water vapor profile
Control	CONTROL	Aircraft observations	None	Background WV profile: smoothed median of WV profiles where AOD < 0.3
Dust only	DU	Aircraft observations	Aircraft observations	Background WV profile: smoothed median of WV profiles where AOD < 0.3
Water vapor only	WV	Aircraft observations	None	Aircraft observations
Dust and water vapor	DU + WV	Aircraft observations	Aircraft observations	Aircraft observations

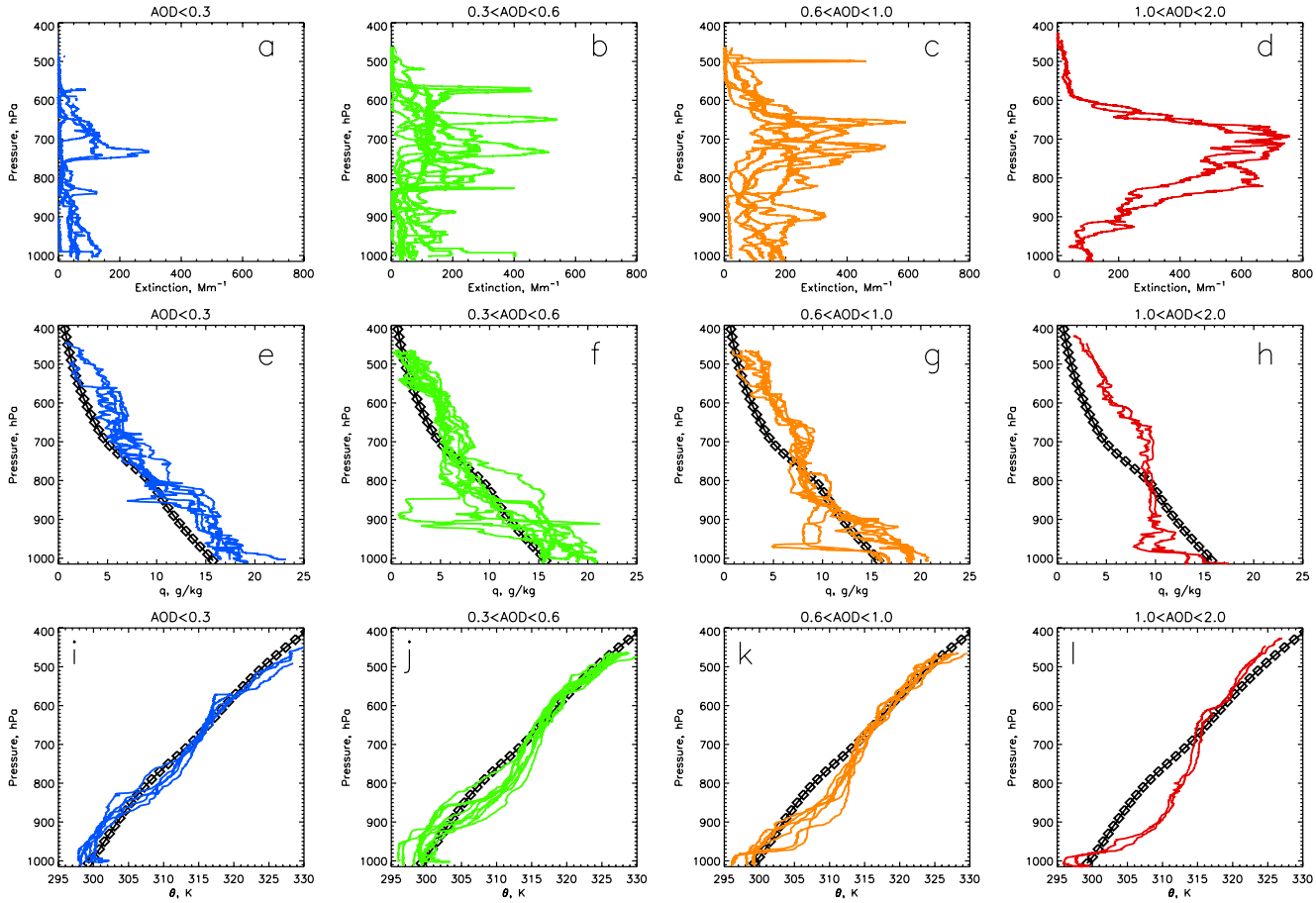

Figure 2. Aircraft profile observations of aerosol extinction (top row), water vapor mixing ratio (middle row) and potential temperature (bottom row). Each variable is subset by measured AOD: blue (AOD < 0.3, 5 profiles), green (0.3 < AOD < 0.6, 9 profiles), orange (0.6 < AOD < 1.0, 6 profiles) and red (AOD > 1.0, 2 profiles). Black diamonds indicate the tropical standard profiles. WV profiles shown in panel (e) are used to create the background WV profile as in Table 2 for the CONTROL experiment.

The direct radiative effect (DRE) due to each experiment relative to the control is calculated as defined in Equation 1.

$$\mathrm{DRE}_{\mathrm{lev}}^{\mathrm{spect}} = \mathrm{NET\_EXPT}_{\mathrm{lev}}^{\mathrm{spect}} - \mathrm{NET\_CONTROL}_{\mathrm{lev}}^{\mathrm{spect}} \quad (1)$$

NET refers to the net (downwards minus upwards) radiative flux at a level (lev) either at the TOA or surface (SFC), for spect which can be either the SW spectrum, LW spectrum, or total (SW + LW). EXPT refers to the experiment in question, either DU, WV, or DU + WV. DREs calculated are instantaneous, diurnally averaged values. Positive values at the TOA indicate a warming of the earth-atmosphere system. The atmospheric (ATM) radiative effect, also sometimes referred to as atmospheric radiative convergence and indicating atmospheric column heating when positive, is calculated from $\mathrm{DRE}_{\mathrm{ATM}}^{\mathrm{spect}} = \mathrm{DRE}_{\mathrm{TOA}}^{\mathrm{spect}} - \mathrm{DRE}_{\mathrm{SFC}}^{\mathrm{spect}}$.

3. Results

3.1. Aircraft Observations of Dust and Water Vapor

Figure 2 shows the profiles of aerosol extinction, WV, and potential temperature observed by the aircraft. Each is subset by the measured AOD, selected so that each range contains a reasonable number of profiles for visualization purposes. The dust load is clearly seen to increase as AOD increases, and the expected vertical profile of the SAL develops, with enhanced dust centered around 700 hPa.

WV profiles are also shown. It is evident that even in cases without much dust (AOD < 0.3, blue), the atmosphere is moister than the tropical standard. It is perhaps not surprising that the measured profiles differ from the tropical standard, given the large amount of variability across tropical regions and the large number of profiles that contribute to the tropical standard atmosphere (e.g., Dunion, 2011).

As AOD increases, the encroachment of the SAL is evident with a deepening of the elevated, near-well-mixed layer. This can also be seen in Figure 3 where medians for each AOD category, and anomalies relative to the background state are shown. As AOD increases, a well-mixed layer of near-constant potential temperature and WV develop, as expected. The near-well-mixed nature of the SAL means that at lower altitudes, the SAL is warmer and drier than the background state, whereas toward the top of the SAL the atmosphere is cooler and moister than the background state.

Figure 3b clearly shows that under increased AODs (or dust loading), enhanced WV in the upper-SAL and decreased WV in the lower-SAL are observed. This becomes more pronounced as the AOD increases. For AODs over 0.6, enhanced WV is observed for heights above 750 hPa, with anomalies exceeding 2 g/kg for the 1 < AOD < 2 category (red line). An interesting double-peaked WV anomaly structure is seen, whereby anomalies peak at a lower level of around 700 hPa, coincident with the center of the SAL and the anomalies it brings, but anomalies also peak at around 500 hPa, due to the dustier SAL cases extending deeper vertically with more moisture at higher altitudes. The increased moisture anomaly only becomes evident across the entire upper SAL at AODs greater than 0.6. For the 0.3–0.6 AOD category, positive anomalies of around 1 g/kg can be seen at heights above 580 hPa, while between 780 and 580 hPa in the upper SAL the air is drier than the reference profile for this AOD category, though the interquartile range does not differ significantly from the zero line.

Dust extinction (Figure 3e) and potential temperature (Figure 3c) as a function AOD are also shown, and show the relatively warmer structure of the SAL becoming more clearly defined as it becomes dustier and closer to being well-mixed, as expected. It is also notable that the highest AOD category (red) shows a cold anomaly in the upper SAL, at heights above 520 hPa.

Dashed lines in Figure 3 show the interquartile range of the profiles in each AOD category up to a value of 1.0. For the WV and potential temperature anomaly profiles (Figures 3b and 3d), although in certain cases and at certain altitudes there is overlap between the categories, a few clear differences are evident. First, in the upper SAL, there is very little overlap in WV mixing ratio interquartile range between the AOD categories, showing a steadily increasing WV anomaly with increasing dust AOD. The dry anomaly at around 800 hPa is clearly different from the zero line (reference case) for all AOD categories, although there is less significance between the dryness of the different categories here due to the large amount of variability in WV in the lower SAL (see also Figures 2f and 2g). In the lower SAL, there is some overlap in the potential temperature anomaly profile between AOD 0.3–0.6 category and AOD 0.6–1 category. However, the AOD > 1 category potential temperature profile clearly lies outside the AOD 0.6–1 category, such that there is a clear progression of increasing potential temperature anomaly with AOD.

To quantify the WV content at various altitudes within the SAL, and relate them to the changing dust AOD, the SAL is separated into the lower and upper SAL, defined as 960–780 hPa and 780–400 hPa, respectively (horizontal dashed lines in Figure 3). These values have been chosen such that the upper SAL covers the pressure range of increased WV anomalies, while the lower SAL covers altitudes below this but excludes the marine boundary layer, evident in Figures 3b, 3d and 3e. Henceforward, the analysis examines the full data set of 22 individual profiles.

Figure 3f shows the relationship between AOD and precipitable water vapor (PWV) for the whole column (black), for the lower SAL (PWV_lower, red), and for the upper SAL (PWV_upper, orange), using the data from individual profiles. Overall, as AOD increases, PWV decreases, though there is a large amount of variability and the linear fit has a low correlation (0.18). More insight is gained into the impact of increased dust through viewing the SAL lower and upper WV changes separately. Figure 3f shows that as AOD increases, PWV_upper increases by 4.4 ± 0.2 mm per unit AOD, while PWV_lower decreases by 5.9 ± 0.4 mm per unit AOD, with the linear fits showing correlations of 0.58 and 0.59, respectively. Uncertainty ranges account for 95% confidence intervals in the slope of the linear fit. In addition, chi-square goodness of fit values of the trends are found to be statistically significant at the 95% confidence level. For the upper SAL, PWV_upper

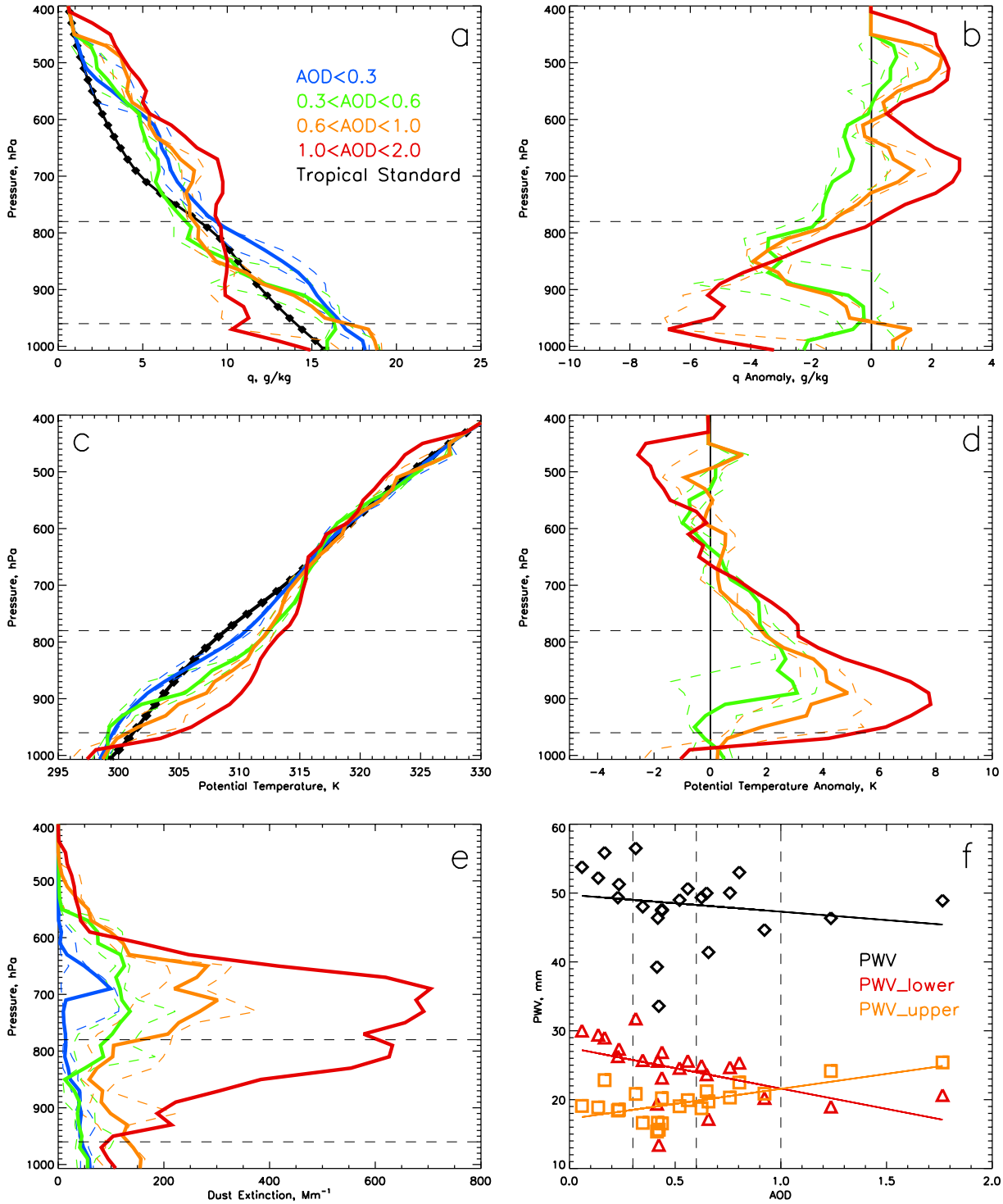

Figure 3. Aircraft observations of (a) Water vapor mixing ratio, (c) Potential temperature and (e) Aerosol extinction; anomalies of (b) Water vapor mixing ratio and (d) Potential temperature relative to the background state (profiles where AOD < 0.3). Profiles are regridded vertically as applied in the RTM. Profiles are grouped by AOD range as indicated with bold lines indicating the median and dashed lines the 25th and 75th percentiles, except for 1 < AOD < 2 where only two profiles contribute to the category. Horizontal dashed lines indicate pressure ranges used for lower and upper SAL definitions. Black line with symbols indicates tropical standard profile. (f) Relationship for all individual profiles between AOD and PWV, PWV_lower ($960 < p > 780$ hPa) and PWV_upper (400 < pressure < 780 hPa), and linear fits, with Pearson's correlation coefficients of 0.18, 0.64, and 0.52, and dPWV/dAOD trend values of -2.4 ± 0.5, -5.9 ± 0.4, and $+4.4 \pm 0.2$ mm/AOD, respectively.

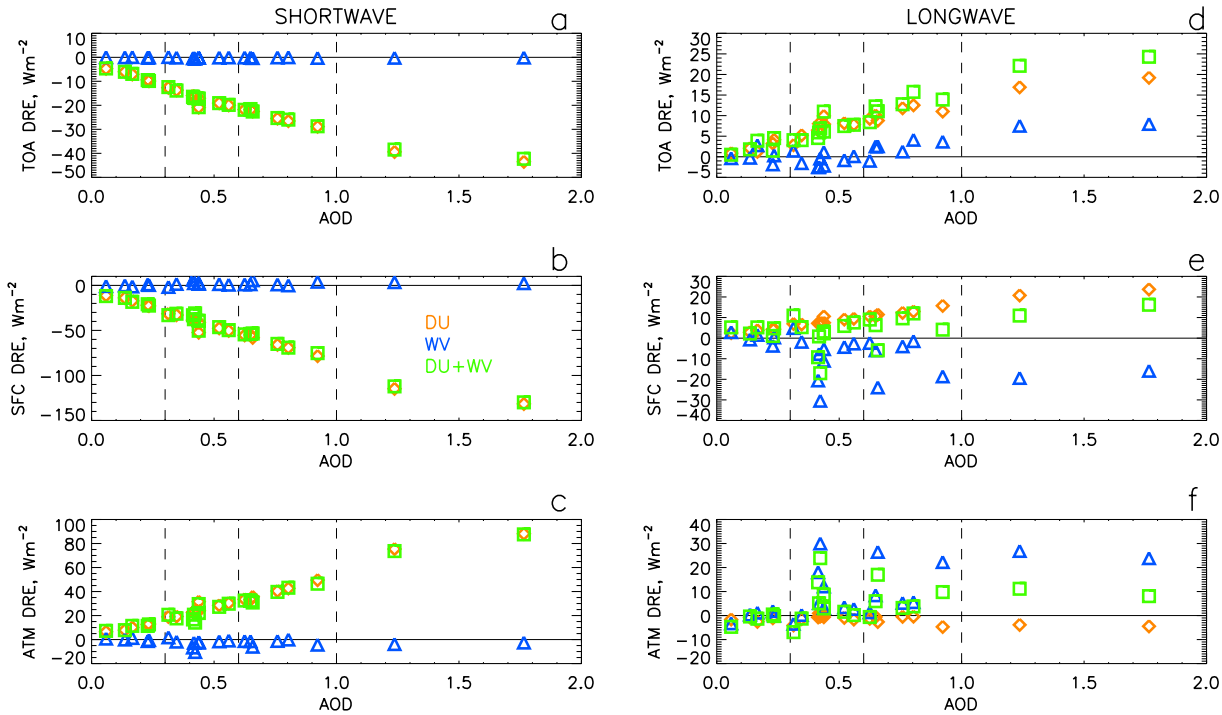

Figure 4. Shortwave (a, b, c; left hand column) and longwave (d, e, f; right hand column) DRE relative to control experiment for the inclusion of dust only (DU, orange), WV only (blue), and dust and WV (DU + WV, green), as a function of 550 nm AOD. Rows show (a, d) DRE at the TOA, (b, d) Surface and (c, f) Atmospheric column. Vertical dashed lines indicate AOD categories.

increases from 18 to 25 mm between the AOD categories of AOD < 0.3 and 1 < AOD < 2, respectively, for the profiles shown in Figure 2a (blue vs. red). Overall, there is a clear relationship between increased dust load (AOD), decreased lower-SAL moisture, and increased upper-SAL moisture.

Although the structure of the SAL has been extensively examined and documented, some of the changes found here are not consistent with the conventional view of the SAL's structure. Figures 2 and 3 show much moister values than those documented in most cases, particularly in the upper SAL of up to 11 g/kg depending on altitude, and with a clear upper SAL moistening with increasing dustiness relative to less dusty cases. Previously, the radiative roles of dust and *dry* SAL air have been assessed (e.g., Wong et al., 2009). Here, we evaluate the radiative effects of the measured dust, and *moist* upper SAL air shown in the observations.

3.2. Impact of Altered WV Structure on Radiative Effect

Having demonstrated that increased dust loadings were associated with increased upper-SAL WV (PWV_upper) but decreased lower-SAL WV (PWV_lower) during AER-D, the DREs from dust only, WV only, and both combined are now described to investigate the radiative impact of the WV changes relative to those from the dust.

Figure 4 shows the SW and LW DRE as a function of AOD for each experiment at the TOA, surface, and atmospheric column. DREs are relative to the CONTROL experiment. The results show that in the SW spectrum, as expected, the main driver of the DRE is always dust, since the WV DREs are comparatively small. Increased dust AOD leads to a more negative TOA DRE, a more negative surface DRE, and larger atmospheric heating, consistent with previous studies.

Figures 4d–4f show the LW DREs as a function of AOD. Here, the WV DRE exerts a large enough effect to alter the DRE significantly. At the TOA dust generates a positive LW DRE (orange points), which increases with AOD. The WV TOA DRE is also mostly positive and also increases with AOD (blue points). This is consistent with increased WV, as observed in the upper-SAL, and will be investigated further in Section 3.3. As a result of the positive DRE due to WV, the DU + WV LW TOA DRE (green data points) is significantly

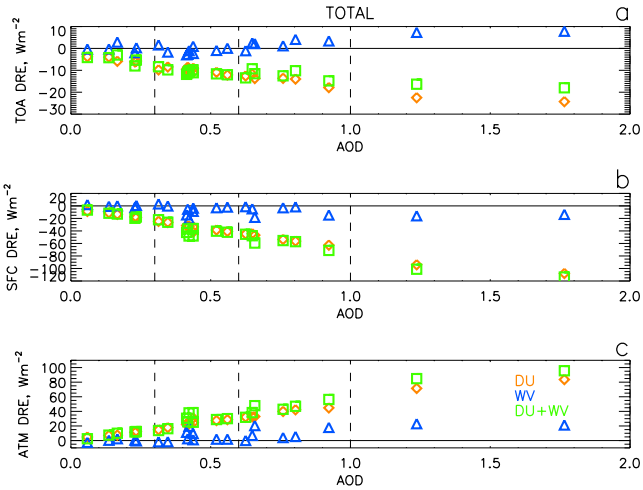

Figure 5. Total (shortwave plus longwave) DRE relative to control experiment for the inclusion of dust only (DU, orange), WV only (blue) and dust and WV (DU + WV, green), as a function of 550 nm AOD. Panels show (a) DRE at the TOA, (b) Surface and (c) Atmospheric column. Vertical dashed lines indicate AOD categories.

larger than due to dust only, with values increasing by an average of 19% or 2.6 ± 0.8 Wm^{-2} when AOD > 0.6 (Values for AOD > 0.6 are given since in this AOD range the changes are most evident, as described in Section 3.1, Figure 3b. Uncertainties given are due to dust optical property sensitivity tests).

At the surface and through the atmospheric column, dust causes a surface warming and an atmospheric cooling. The WV DRE is the opposite, resulting in a negative surface DRE and atmospheric heating. This is consistent with a net reduction in WV, and Section 3.3 will demonstrate that these changes are driven by a reduction in lower-SAL WV. At the surface, this results in a reduced LW DRE from DU + WV compared to DU alone, with values reducing by 49% or 7.0 ± 0.5 Wm^{-2} on average when AOD > 0.6. In the atmosphere, WV changes the sign of atmospheric heating, from a mean of −2.3 Wm^{-2} for DU to +7.3 Wm^{-2} for DU + WV when AOD > 0.6, an increase of 9.6 ± 0.5 Wm^{-2}.

Figure 5 shows the total (SW + LW) DREs as a function of AOD. The total TOA DRE for dust is negative, while the WV TOA DREs are positive, driven by positive LW DREs. The net effect of including the observed WV profiles is to reduce the magnitude of the total negative DRE for DU + WV compared to DU alone. Overall, when AOD > 0.6, including WV effects increases the mean TOA DRE from dust by 3.0 ± 0.8 Wm^{-2} or decreases the magnitude of the negative DRE by 17%.

Figure 5 shows that at the surface, the main driver of the total DRE is dust. WV DREs at the surface are small and negative and reduce the SFC DRE by a mean of 8% or 5.1 ± 0.8 Wm^{-2} for DU + WV compared to DU when AOD > 0.6.

In the atmospheric column, dust is also the main driver of total atmospheric heating. However, here the WV change acts to enhance this heating by 8.0 ± 0.6 Wm^{-2} or 17% when AOD > 0.6, as a result of the LW WV effect.

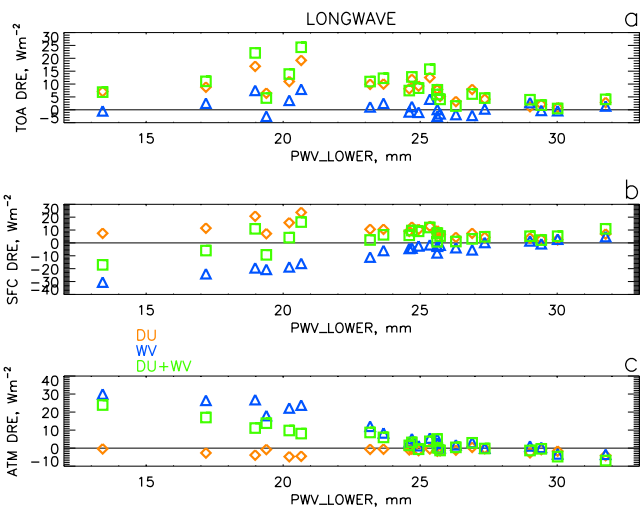

Figure 6. Longwave DRE relative to control experiment, as a function of the lower SAL PWV (PWV_lower), for the inclusion of dust only (DU, orange), WV only (blue) and dust and WV (DU + WV, green). Panels show (a) DRE at the TOA, (b) Surface and (c) Atmospheric column.

3.3. Impact of WV in the Lower and Upper-SAL

Figure 6 and 7 show the LW DREs as a function of PWV in the lower and upper SAL, respectively, to isolate the impacts of the changed WV structure with increasing dust, whereby WV in the upper-SAL increases, but decreases in the lower-SAL.

In Figure 6, clear relationships between PWV_lower and both surface and atmospheric LW DRE can be seen for WV (blue data points), but not at the TOA. In the atmosphere (panel c), a drier lower-SAL results in relatively more atmospheric heating (or equivalently less atmospheric cooling), while at the surface, drier lower-SAL conditions result in a more negative LW DRE because less radiation is emitted downwards by the drier atmosphere.

Under dustier conditions when the lower-SAL is drier, the DU experiment mostly results in slightly negative LW ATM DRE values (atmospheric cooling, orange points in Figure 6c). The addition of the WV DRE changes is large enough to change the sign of ATM DRE and result in atmospheric heating for DU + WV (green points). Thus the change in sign from cooling to heating (also seen in Figure 4f) for DU + WV compared to DU is explained by lower moisture content in the lower-SAL, and the LW ATM DRE for WV increases as moisture in the lower-SAL decreases. In Figure 6b drier, dustier lower-SAL results in a positive surface

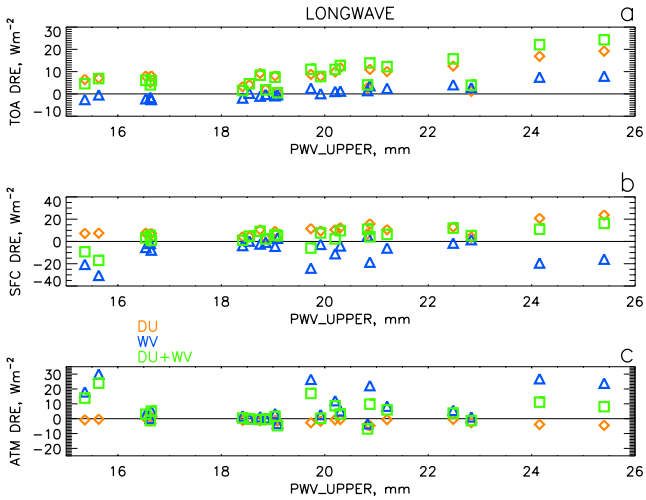

Figure 7. Longwave DRE relative to control experiment, as a function of the upper SAL PWV (PWV_upper), for the inclusion of dust only (DU, orange), WV only (blue) and dust and WV (DU + WV, green). Panels show (a) DRE at the TOA, (b) Surface and (c) Atmospheric column.

DRE for DU. Since the WV surface DRE is negative, values for DU + WV are sometimes large enough to change the LW sign compared to DU. In contrast the TOA DRE shows no dependence on WV in the lower SAL in Figure 6a.

Figure 7 shows the DREs as a function of PWV in the upper-SAL. Although PWV_upper has no observable effect over the LW DRE at the surface and on the total atmospheric column, it has a strong effect on the LW DRE at the TOA. Larger PWV_upper (associated with increased dustiness) results in larger, more positive LW TOA DREs due to reduced outgoing LW radiation. This is seen for both the WV and DU experiments. When WV in the upper-SAL is higher, its proximity to the TOA (compared to the lower SAL) means that enhanced upper-SAL WV results in less LW radiation being emitted and therefore a warming effect results. At the same time, since dust AOD and PWV_upper are related, the LW dust TOA DRE also increases for high PWV_upper values. As a result, the two effects act in the same direction and increase the DU + WV TOA DRE.

This also explains the trend seen in Figure 4d, and confirms that the TOA WV effect is controlled by changes to PWV_upper, rather than PWV_lower, as emphasized by previous studies. Thus increases in dust and increased PWV_upper both act to cause and amplify a positive LW TOA DRE.

Figure 8 shows the absolute heating rates for the control and changes in heating rates for each experiment for the SW, LW, and total relative to the control. It can be seen that dust (Figures 8d–8f) causes a SW heating, a LW cooling, and a total heating. In the SW, WV (Figure 8g) causes a slight heating at higher altitudes which is stronger and higher for larger AOD where PWV_upper is larger. In the LW (Figure 8h), the impact of increased PWV_upper and decreased PWV_lower can be seen. When AODs are higher, more upper-SAL cooling from enhanced moisture and less mid-SAL cooling (i.e., warming) from enhanced dryness is observed. This results in changes to total heating rates of up to −2.5 K/d in the upper SAL and +1.5 K/d through the lower-SAL due to the dust-related WV changes (Figure 8i).

Comparing Figure 8f to Figure 8l shows the changes in total heating rates due to DU + WV compared to dust alone. We see that the total WV + DU heating rates (panel l) show extra cooling at heights above 550 hPa and increased heating through the mid-SAL (~950–600 hPa), higher by about 1 K/d relative to panel f. Although increased dust was associated with decreased PWV_lower at heights beneath 780 hPa, the radiative heating effects of this WV change are felt throughout the wider column up to around 680 hPa. As a result, the PWV_lower changes control the ATM DRE, determining atmospheric heating or cooling, as shown in Figure 5c. It is also notable that only by including the enhanced WV in the upper SAL, is the cold anomaly in potential temperatures seen in Figure 3d consistent with the additional cooling rates above around 500 hPa.

4. Discussion

This study finds elevated moisture levels in the upper SAL associated with dust, and demonstrates that this increased moisture is important in determining the magnitude, and potentially the sign of the radiative effect exerted by the dusty SAL. The elevated moisture found in the upper SAL differs to the frequently reported SAL characteristics of it being a straightforward dry layer, suggesting that more complexity and vertical detail is required to accurately reflect the SAL and its radiative impacts.

4.1. Structure of the SAL

Much previous work characterizing the SAL focuses on its lower atmospheric structure, particularly heating rates at around 850 hPa and their relation to sustaining the temperature inversion between the MBL and the SAL base, due to its importance in suppression of convection and potentially impeding tropical cyclone

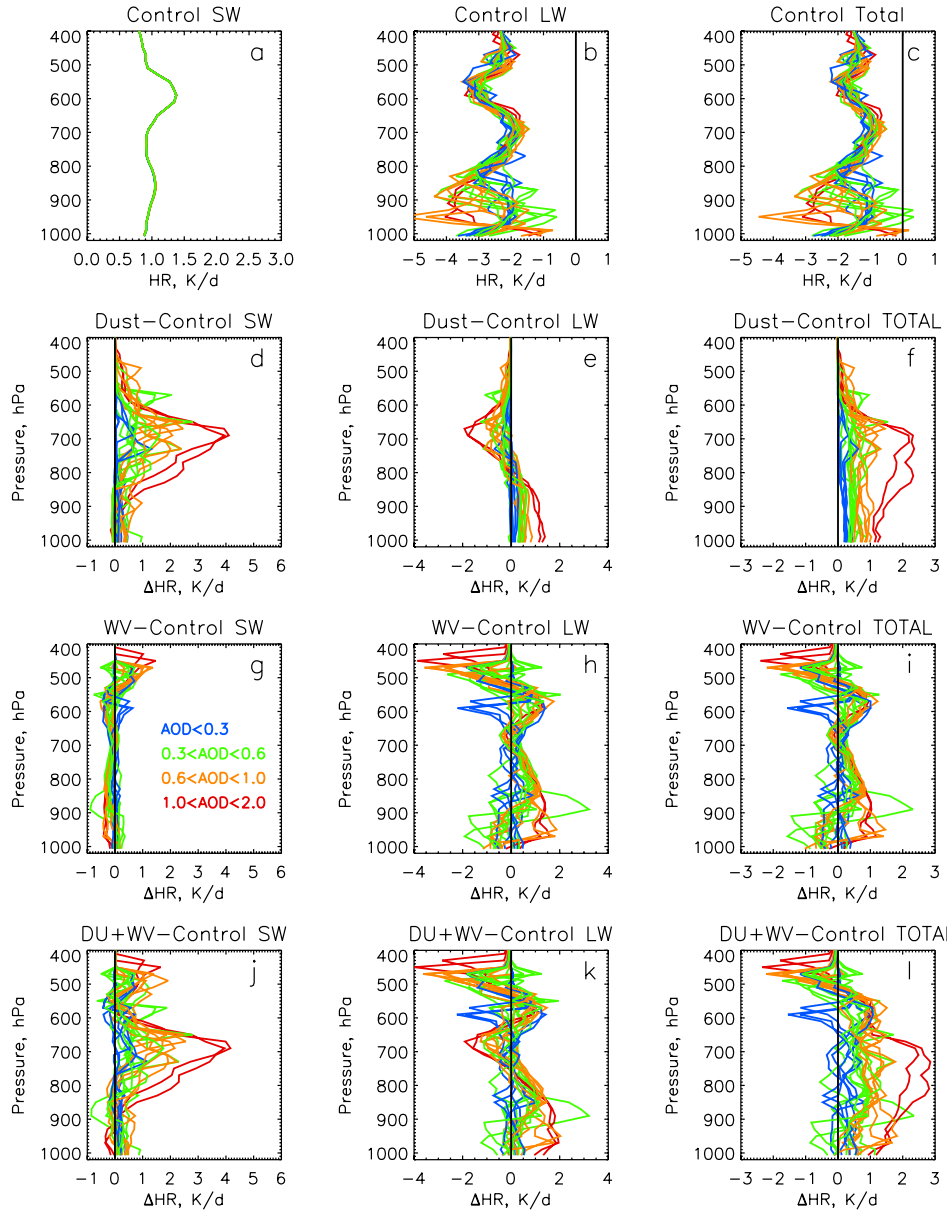

Figure 8. Top row: absolute heating rates for the CONTROL for all profiles for (a) SW, (b) LW, (c) Total (SW + LW). Other rows: changes in heating rates (HR, K/day) between each experiment and the control, for (d)–(f) DU, (g)–(i) WV (middle row), and (j–l) WV + DU (bottom row), for the SW spectrum (left), LW spectrum (center), and total (SW plus LW, right). Profiles are colored as a function of AOD.

development (e.g., Dunion & Velden, 2004; Wong et al., 2009). However, a few studies have focused more on the structure of the entire depth of the SAL. For example, Braun (2010) find a 400–600 hPa moistening across Africa to Saudi Arabia relative to the very dry Saharan air below, due to deep, dry convective mixing over the Sahara. This structure has sometimes been found at the west coast of Africa and also downstream. Ismail et al. (2010) show a case where WV mixing ratios were around 2–7 g/kg throughout the SAL. They attribute this increased moisture to midaltitude convection as a result of intensification of an AEW, pointing out that increased WV leaves the SAL more amenable to convection. Thus the elevated WV in the upper SAL may have a wider dynamical impact than has been possible to examine here.

Despite the fact that the observations presented here show enhanced moisture in the upper-SAL compared to background conditions, we do not suggest that the SAL deviates from being a near-well-mixed, elevated

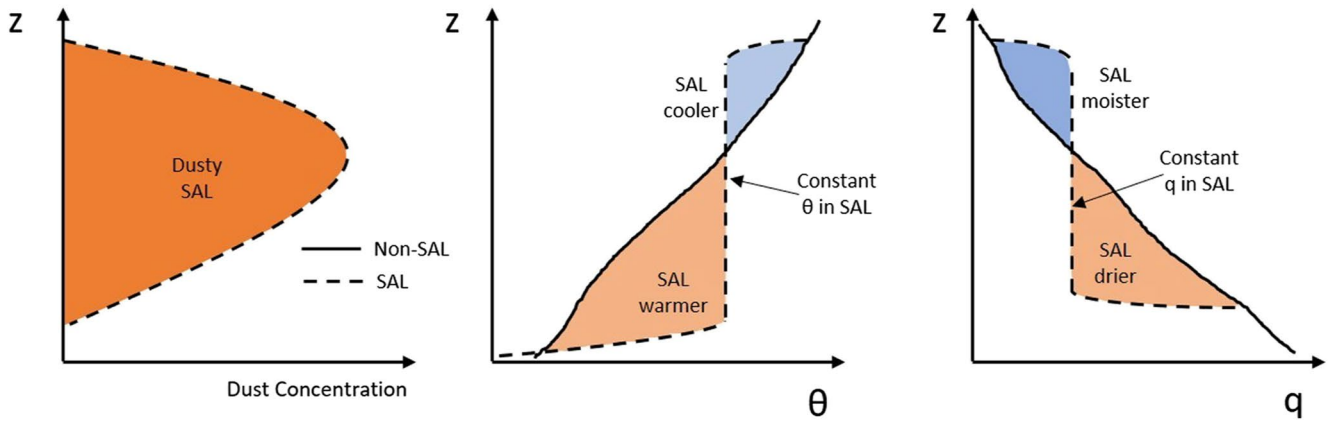

Figure 9. Idealized schematic depicting anomalies observed in the dusty SAL. SAL conditions are characterized by near-constant potential temperature (θ) and water vapor mixing ratios (q). Compared to the background, non-SAL environment, this results in a warmer, drier lower-SAL and a cooler, moister upper-SAL.

layer. This is illustrated through the schematic shown in Figure 9, which is based on the observations shown in Figure 3. The background (non-SAL) profiles of potential temperature and WV mixing ratio are represented by gradually increasing and decreasing values, respectively. Therefore, when a near-well-mixed layer (the SAL), with near-constant potential temperature and WV mixing ratio, is imposed, this results in either a positive or negative anomaly in both its upper and lower portions. Therefore, the results presented in this study do not oppose the previous documentation of the SAL evidencing its well-mixed nature, they simply expose the extension of the well-mixed SAL upwards which results in the cooler, moister upper-SAL anomalies shown in Figure 9. The absolute magnitude of WV mixing ratios in the SAL will determine the magnitude of the anomalies relative to the background condition, such that a moister, well-mixed SAL would shift the line of constant q shown in Figure 9 to the right, increasing the moist anomaly.

It is important to note that several relevant previous studies have not found the elevated positive moisture anomaly shown in Figure 9, though they do report all the other features. For example, Wong et al. (2009) utilized satellite and reanalysis data covering 2003–2006. They found a dry anomaly in the lower SAL at ~850 hPa over the Eastern tropical Atlantic, but did not find evidence of a moist anomaly in the upper SAL, though they did find a cold temperature anomaly at 500 hPa, similar to this study. Therefore their findings support most of the anomalies shown in the schematic in Figure 9 except the upper SAL positive moisture anomaly. Similarly, Dunion (2011) examined thousands of rawinsondes covering 1995–2002 in the Caribbean region, but did not find an upper SAL positive moisture anomaly. However, they stress that their results are only representative of the western tropical Atlantic, not the eastern tropical Atlantic, as presented here. Nevertheless, the findings of Gutleben et al. (2019, 2020), which show enhanced WV in the SAL over the western Atlantic, indicate that the results in this manuscript are not an isolated result.

Gutleben et al. (2019) present airborne observations from a case study in the western Atlantic SAL. They find that WV mixing ratios increased in the SAL relative to the free troposphere, and their results show that the increase from dry to moist air descending into the top of the SAL is important for driving strong LW cooling rates at the top of the SAL, similar to the heating rate profiles shown here. Their analysis used the tropical standard profile to isolate the impact of changing WV, though a comparison to this study is not straightforward, since the SAL was actually drier than the tropical standard in that study. Gutleben et al. (2020) extended this research and found that heating rates from dust only were small (net warming of ~0.3 K/day) in comparison to total heating rates. These values are lower than found in this study for dust only (~0.5–2.5 K/day), though using comparable AODs of 0.3 and lower, we find comparable heating rates here. However, although they linked changes in the total heating rate profile to enhanced WV in the SAL, no experiments were performed to explicitly isolate the radiative effect of WV.

Enhanced moisture has also been found in biomass burning aerosol (BBA) layers (Adebiyi et al., 2015; Pistone et al., 2021). Adebiyi et al. (2015) show that anomalous moisture in BBA layers over the southeast Atlantic leads to anomalous LW cooling in the layer counteracting the SW heating from the BBA. However, due to the negligible LW radiative effect of BBA, the LW and SW radiative effects of WV combine differently

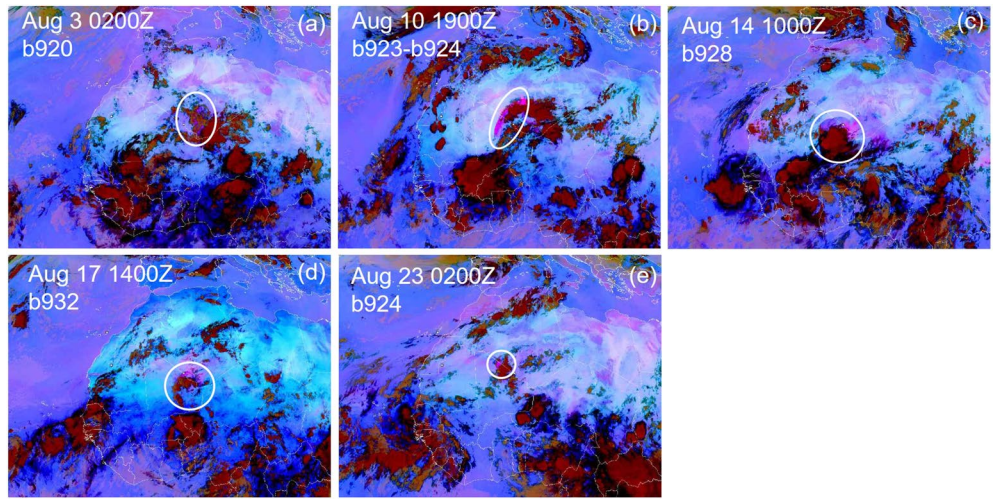

Figure 10. MSG SEVIRI RGB Dust false color satellite imagery showing cold pool outflows driving dust uplift in the form of haboobs, preceding the dust events studied. Dark red colors indicate deep cloud, orange is mid-level cloud, dull pink is low level cloud. Dust appears bright pink to purple. Panel labels indicate date and time of the image shown and the flight to which they correspond. White circles indicate the haboob location.

in the results of Adebiyi et al. (2015) to those presented here. Clearly dust layers are not the only type of aerosol layer which can be collocated with enhanced WV, and there may be more instances of transported aerosol layers globally where WV changes exert an effect.

As well as influencing the radiative effect, enhanced upper SAL moisture and associated cooling at these altitudes may also influence mid-level altocumulus cloud development. For example, it could be important to the development of the frequently observed altocumulus cloud capping the SABL and SAL, as shown in Kealy et al. (2017) and Mantsis et al. (2020), which play an important radiative role.

The additional cooling at the top of the SAL due to WV may help to maintain its well-mixed vertical structure, aiding subsidence at the SAL top, combined with ascent at the SAL base due to the well-known lower SAL heating from both dust and WV. This is consistent with a lowering of the SAL top toward the west, and a rising of the SAL base (e.g., Liu et al., 2008; Tsamalis et al., 2013).

4.2. Origins of the Observed Dust and Water Vapor

We stress that the observed WV profile is not caused by the presence of dust, but rather both the dust and WV profile structures are likely driven by dynamical features influencing both initial dust uplift and the SAL. Indeed, all the dust events sampled were initiated (at least in part) by cold pool outflows from deep convection, driving haboobs. Figure 10 shows satellite imagery for each dust event at the time when dust uplift related to cold pool outflows occurred. Images are from Meteosat Second Generation (MSG) Spinning Enhanced Visible and InfraRed Imager (SEVIRI), for the red-green-blue (RGB) thermal infrared dust product (Brindley et al., 2012), where dust typically appears as bright pink. Dust sources for the dust sampled during AER-D were identified by Ryder et al. (2018) using the high temporal resolution (15 min) of the MSG imagery and manually backtracking the dust in time (Back trajectories were not used due to the poor representation of winds in reanalyses over the summertime Sahara [Roberts et al., 2017], as discussed in Ryder et al. [2018]). In all cases, at least one (and sometimes several) cold pool outflows, leading to haboobs, were identified as the meteorological driver for the dust uplift. This can be seen in Figure 10 by the proximity of the dust shown in the white circles to the deep convective cloud (red), frequently spreading out in a radial pattern typical of haboobs. In many of the cases, cloud partly or totally (Figure 10a) covers the dust, though the dust is identifiable in the animated imagery (not shown).

It is well known that dust uplifted by cold pool outflows is associated with elevated moisture levels (Marsham et al., 2013), and that cold pool outflows play a key role in the transport of both WV and dust into the SHL region (Allen et al., 2013; Engelstaedter et al., 2015; Flamant et al., 2007; Marsham et al., 2013; Yu

et al., 2021) where both are mixed throughout the deep Saharan boundary layer, before being transported westwards within the SAL. Given that all the events sampled here were driven by cold pool outflows, it seems likely that the enhanced moisture measured by the aircraft derives from the dominance of cold pool outflows as the meteorological dust uplift mechanism. Strong winds associated with cold pool outflows, embedded within monsoon surges, likely drove strong dust emission at the same time as transporting WV northwards toward the SHL region, as described by Marsham et al. (2013). Thus it appears that cold pool outflows hold a key role in determining dust and WV characteristics in both the Saharan region as well as downstream in the SAL. Further detailed investigation into the WV transport is beyond the scope of this article, though a larger scale regional and temporal analysis of the relationship between dust uplift and moisture transport from cold pool outflows, their behavior over the Sahara and during further westward transport over the Atlantic Ocean would be invaluable.

An interesting question regarding elevated moisture in the upper SAL is whether this is a feature that has simply been under-investigated in the past, or whether the moistening is a temporal trend. Evan et al. (2015) show that WV content in the SHL region over Africa has increased over the last 30 years as a result of a WV-temperature feedback cycle. Thus it seems plausible that the SAL, outflowing from the Sahara, may be moistening as a consequence. Given the key role of cold pool outflows and haboobs in the transport of WV and dust into the SHL region before onwards transport to the SAL (Allen et al., 2013; Engelstaedter et al., 2015; Flamant et al., 2007; Marsham et al., 2013; Yu et al., 2021), another question which arises is whether the intensity and/or frequency of cold pool outflows over west Africa has changed over time.

4.3. WV and Transport of Coarse Dust

The ability of enhanced moisture in the upper-SAL to reduce the magnitude of the negative TOA radiative effect of the SAL, shifting it toward positive values, is particularly important when considered with other recent developments in the literature. Adebiyi and Kok (2020) have shown that climate models miss most coarse dust in the atmosphere, and including this missed coarse dust adds a TOA radiative warming effect of 0.15 Wm^{-2} globally. Di Biagio et al. (2020) show that updated dust optical properties and inclusion of dust sizes larger than 20 μm further shifts the global DRE of dust away from a cooling effect, to -0.03 Wm^{-2}. When combined with potential increases in upper SAL moisture, this will further shift the regional radiative effect of dust toward a net warming effect over the tropical Atlantic. The importance of these combined effects will be further increased in regions where dust emissions are increasing over time, exerting a radiative forcing that may tend toward positive values.

Another pertinent question concerns potential mechanisms which may enable coarse dust particles to be transported further than expected (Mallios et al., 2020; O'Sullivan et al., 2020; Ryder et al., 2019; van der Does et al., 2018; Weinzierl et al., 2017). This study shows that as well as a significant day-time SW atmospheric column heating from dust, the reduced lower-SAL moisture which occurs under dustier conditions can lead to increased atmospheric LW heating throughout most of the SAL depth, which will dominate at night. Both these mechanisms may contribute to continual diurnal upward dynamic effects which may increase the lifetime and long-range transport of dust particles, including the coarser sizes (rather than a vertical mixing occurring during daytime followed by night-time settling, as explored in Gasteiger et al., 2017).

4.4. Limitations and Uncertainties

Finally, there are several uncertainties and limitations inherent in this study. First, the main uncertainty stems from the observations consisting of a limited number of 22 profiles only representing August 2015 and the eastern Tropical Atlantic region. It is clear that a wider spatial and temporal analysis would be beneficial. For example, questions such as whether the upper-SAL WV enhancement is present throughout the summer dust season, how this varies depending on cold pool outflow and convective activity over the continent and how WV structure may vary year to year and westwards across the Atlantic are important. These questions would benefit from analyses covering a wider geographic region and longer temporal period than has been possible here, such as employing satellite data and/or reanalysis, updating the study of Wong et al. (2009).

Nevertheless, there are benefits to the in-situ, aircraft measurement-based approach used here, which are not possible via larger scale satellite and/or reanalysis approaches. For example, the aircraft data provide measurements at high vertical resolution of dust burden and WV mixing ratios, which are perfectly co-located. This allows the co-located optical properties of the dust to be sampled. This level of detail would not be possible using other data sets such as satellite retrievals or reanalyses, and concurrent high-quality information of height-resolved dust optical properties would not be available. For example, the study of Wong et al. (2009) relied on model simulations of the vertical distribution of dust and size distributions. Finally, despite the number of profiles here being limited, a wide range of AODs (0.06–1.8) are sampled.

A second uncertainty in this study stems from the optical properties of the dust applied in the RTM, which were setup specifically to match the in-situ size and composition results measured during the AER-D campaign (Ryder et al., 2018). As a sensitivity study, optical properties were also selected to represent more extreme values of absorbing dust and less absorbing dust, representing a range of dust optical properties that have been applied in climate models. The impact of the WV perturbation to the DRE is quite sensitive to the optical properties assumed (see Figures S1–S3 in Supporting Information S1). For example, at the TOA, the total DRE due to dust approaches zero when dust is very absorbing in the SW. Therefore, when the WV changes are also included, which are positive, the final TOA DRE from DU + WV can sometimes change sign, becoming positive. Conversely, for less absorbing dust with a high SSA, the dust DRE at the TOA is more negative. Therefore, proportionally, the addition of a positive WV DRE results in a smaller fractional decrease in the negative DRE. Nevertheless, whatever the chosen optical properties of dust are, the radiative changes due to the WV profile remain important.

Finally, this work does not account for any changes in humidity upon the microphysical properties of the dust, such as possible hygroscopic growth and changes in scattering properties. Although it is possible that hydrophobic dust particles become more hygroscopic during transport through chemical coatings such as sulfate, there is much uncertainty in understanding of this process and some studies show that this is not an important factor during trans-Atlantic dust transport (Denjean et al., 2015). Additionally, measurements of scattering and absorption at different humidities were not taken during AER-D.

5. Conclusions

This study presents results from 22 in-situ aircraft profiles sampling dust events over the eastern tropical Atlantic during August 2015. The dust events were driven largely by cold pool outflows from deep convection, driving haboobs. It has been shown that as dust loadings increase and the thermal characteristics of the SAL develop, WV mixing ratios decrease in the lower-SAL (960–780 hPa) and increase in the upper SAL (780–400 hPa) at a mean rate of 4.4 ± 0.2 mm per unit AOD.

Conventionally the SAL is considered to be a warm, dry, elevated, well-mixed layer that is frequently dusty (e.g., Carlson & Prospero, 1972). Therefore the observations of enhanced moisture in the upper SAL under dusty conditions are somewhat contradictory to this description. This can be reconciled by observations presented here showing that the SAL has near-well-mixed characteristics, but by extending them upwards in altitude, where the SAL then becomes cooler and moister than the background conditions.

The radiative impact of the observed WV and dusty profiles have been quantified using an RTM. The enhanced upper-SAL moisture was found to have the most effect at the TOA, causing a positive DRE, counteracting the negative TOA DRE exerted by the dust. When both WV and dust were included, the negative DRE at the TOA from dust was reduced in magnitude by a mean of 17% (3.0 ± 0.8 Wm^{-2}) for AODs larger than 0.6. Thus, accounting for the complex WV profile is crucial in determining the radiative effect of the dusty SAL, and is significantly different to simply assuming a dry profile.

The total DRE at the surface and in the atmosphere were dominated by dust effects, but were enhanced by WV reductions in the lower-SAL. Decreases in lower-SAL WV acted to increase the magnitude of the negative surface DRE from dust by 8% (5.1 ± 0.8 Wm^{-2}) and increase atmospheric heating by 17% (8.0 ± 0.6 Wm^{-2}) on average for AODs > 0.6.

Changes in the total DRE were driven by WV changes from the LW spectrum. Less WV in the lower-SAL under dusty conditions resulted in a more negative surface LW DRE due to less emission of LW radiation

from WV toward the surface from the lower-SAL. At the same time, less LW cooling occurred in the drier lower-SAL due to smaller LW absorption. In the LW spectrum, the inclusion of the dry lower-SAL results in change in sign from net cooling to net heating for the atmospheric column compared to dust only, and could be important for nighttime dynamics and dust transport within the SAL.

Heating rate profile changes due to WV and dust in the SAL were calculated. Dust was found to cause a net heating, driven by SW heating, whereas the WV structure generated cooling in the upper-SAL and heating throughout the mid to lower-SAL compared to background conditions, amplifying the heating occurring here due to dust. The upper-SAL cooling under dustier conditions due to WV is consistent with colder upper SAL temperatures in dusty conditions.

Although this study only represents dust events in the SAL from August 2015, increased moisture in the SAL is consistent with an observed moistening of the SHL region over west Africa over the last 30 years as part of a feedback cycle driven by increased temperatures (Evan et al., 2015). All the events sampled here were influenced by convective cold pool outflows, driving dust uplift and haboobs, as well as transporting WV toward the Sahara, and eventually westwards to the SAL. It is well known that cold pool outflows play a crucial role in transporting WV into the SHL region (Allen et al., 2013; Engelstaedter et al., 2015; Flamant et al., 2007; Marsham et al., 2013). Therefore future work should evaluate the prevalence of moisture on wider temporal and spatial scales than has been possible here, and also examine whether there are temporal trends in the transport of WV and dust northwards into the Sahara by cold pool outflows, potentially as a result of climate change, as well as examining the ability of models with explicit dust schemes to reproduce the dust-WV relationship shown here.

Data Availability Statement

Aircraft data are available at the Center for Environmental Data Archive at http://catalogue.ceda.ac.uk/uuid/d7e02c75191a4515a28a208c8a069e70.

Acknowledgments
C. L. Ryder received funding from NERC Independent Research Fellowship NE/M018288/1. Airborne data from the BAe 146 were obtained using the BAe 146–301 Atmospheric Research Aircraft operated by Directflight Ltd and managed by FAAM, which was a joint entity of the NERC and the UK Met Office. K. Shine, R. Herbert, and F. Marenco are thanked for useful discussions relating to this study.

References

Adebiyi, A. A., & Kok, J. F. (2020). Climate models miss most of the coarse dust in the atmosphere. *Science Advances*, *6*(15), eaaz9507. https://doi.org/10.1126/sciadv.aaz9507

Adebiyi, A. A., Zuidema, P., & Abel, S. J. (2015). The convolution of dynamics and moisture with the presence of shortwave absorbing aerosols over the Southeast Atlantic. *Journal of Climate*, *28*(5), 1997–2024. https://doi.org/10.1175/Jcli-D-14-00352.1

Allen, C. J. T., Washington, R., & Engelstaedter, S. (2013). Dust emission and transport mechanisms in the central Sahara: Fennec ground-based observations from Bordj Badji Mokhtar, June 2011. *Journal of Geophysical Research: Atmospheres*, *118*(12), 6212–6232. https://doi.org/10.1002/jgrd.50534

Anderson, G. P., Clough, S. A., Kneizys, F. X., Chetwynd, J. H., & Shettle, E. P. (1986). AFGL atmospheric constituent profiles (0–120 km). In Technical Report AFGL-TR-86-0110, AFGL (OPI), Hanscom. (AFB, MA. 01736).

Balkanski, Y., Schulz, M., Claquin, T., & Guibert, S. (2007). Reevaluation of mineral aerosol radiative forcings suggests a better agreement with satellite and AERONET data. *Atmospheric Chemistry and Physics*, *7*, 81–95. https://doi.org/10.5194/acp-7-81-2007

Braun, S. A. (2010). Reevaluating the role of the Saharan air layer in Atlantic tropical cyclogenesis and evolution. *Monthly Weather Review*, *138*(6), 2007–2037. https://doi.org/10.1175/2009mwr3135.1

Brindley, H., Knippertz, P., Ryder, C., & Ashpole, I. (2012). A critical evaluation of the ability of the Spinning Enhanced Visible and Infrared Imager (SEVIRI) thermal infrared red-green-blue rendering to identify dust events: Theoretical analysis. *Journal of Geophysical Research: Atmospheres*, *117*, D07201. https://doi.org/10.1029/2011jd017326

Carlson, T. N. (2016). The Saharan elevated mixed layer and its aerosol optical depth. *The Open Atmospheric Science Journal*, *10*, 26–38. https://doi.org/10.2174/1874282301610010026

Carlson, T. N., & Benjamin, S. G. (1980). Radiative heating rates for Saharan dust. *Journal of the Atmospheric Sciences*, *37*(1), 193–213. https://doi.org/10.1175/1520-0469(1980)037<0193:Rhrfsd>2.0.Co

Carlson, T. N., & Prospero, J. (1972). The large-scale movement of Saharan air outbreaks over the Northern Equatorial Atlantic. *Journal of Applied Meteorology and Climatology*, *11*(2), 283–297. https://doi.org/10.1175/1520-0450(1972)011<0283:TLSMOS>2.0

Colarco, P. R., Nowottnick, E. P., Randles, C. A., Yi, B. Q., Yang, P., Kim, K. M., et al. (2014). Impact of radiatively interactive dust aerosols in the NASA GEOS-5 climate model: Sensitivity to dust particle shape and refractive index. *Journal of Geophysical Research: Atmospheres*, *119*(2), 753–786. https://doi.org/10.1002/2013jd020046

Cusack, S., Edwards, J. M., & Crowther, J. M. (1999). Investigating k distribution methods for parameterizing gaseous absorption in the Hadley Centre Climate Model. *Journal of Geophysical Research: Atmospheres*, *104*(D2), 2051–2057. https://doi.org/10.1029/1998jd200063

Denjean, C., Caquineau, S., Desboeufs, K., Laurent, B., Maille, M., Rosado, M. Q., et al. (2015). Long-range transport across the Atlantic in summertime does not enhance the hygroscopicity of African mineral dust. *Geophysical Research Letters*, *42*(18), 7835–7843. https://doi.org/10.1002/2015gl065693

Di Biagio, C., Balkanski, Y., Albani, S., Boucher, O., & Formenti, P. (2020). Direct radiative effect by mineral dust aerosols constrained by new microphysical and spectral optical data. *Geophysical Research Letters*, *47*(2), e2019GL086186. https://doi.org/10.1029/2019GL086186

Doherty, O. M., & Evan, A. T. (2014). Identification of a new dust-stratocumulus indirect effect over the tropical North Atlantic. *Geophysical Research Letters*, *41*(19), 6935–6942. https://doi.org/10.1002/2014gl060897

Dubovik, O., Holben, B., Eck, T. F., Smirnov, A., Kaufman, Y. J., King, M. D., et al. (2002). Variability of absorption and optical properties of key aerosol types observed in worldwide locations. *Journal of the Atmospheric Sciences*, *59*(3), 590–608. https://doi.org/10.1175/1520-0469(2002)059<0590:Voaaop>2.0.Co

Dunion, J. P. (2011). Rewriting the climatology of the Tropical North Atlantic and Caribbean Sea Atmosphere. *Journal of Climate*, *24*(3), 893–908. https://doi.org/10.1175/2010jcli3496.1

Dunion, J. P., & Velden, C. S. (2004). The impact of the Saharan air layer on Atlantic tropical cyclone activity. *Bulletin of the American Meteorological Society*, *85*(3), 353–366. https://doi.org/10.1175/Bams-85-3-353

Edwards, J. M., & Slingo, A. (1996). Studies with a flexible new radiation code. 1: Choosing a configuration for a large-scale model. *Quarterly Journal of the Royal Meteorological Society*, *122*(531), 689–719. https://doi.org/10.1002/qj.49712253107

Engelstaedter, S., Washington, R., Flamant, C., Parker, D. J., Allen, C. J. T., & Todd, M. C. (2015). The Saharan heat low and moisture transport pathways in the central Sahara-Multiaircraft observations and Africa-LAM evaluation. *Journal of Geophysical Research: Atmospheres*, *120*(10), 4417–4442. https://doi.org/10.1002/2015jd023123

Evan, A. T., Flamant, C., Lavaysse, C., Kocha, C., & Saci, A. (2015). Water vapor-forced greenhouse warming over the Sahara desert and the recent recovery from the Sahelian drought. *Journal of Climate*, *28*(1), 108–123. https://doi.org/10.1175/Jcli-D-14-00039.1

Flamant, C., Chaboureau, J. P., Parker, D. J., Taylor, C. A., Cammas, J. P., Bock, O., et al. (2007). Airborne observations of the impact of a convective system on the planetary boundary layer thermodynamics and aerosol distribution in the inter-tropical discontinuity region of the West African Monsoon. *Quarterly Journal of the Royal Meteorological Society*, *133*(626), 1175–1189. https://doi.org/10.1002/Qj.97

Gasteiger, J., Groß, S., Sauer, D., Haarig, M., Ansmann, A., & Weinzierl, B. (2017). Particle settling and vertical mixing in the Saharan Air Layer as seen from an integrated model, lidar, and in situ perspective. *Atmospheric Chemistry and Physics*, *17*, 297–311. https://doi.org/10.5194/acp-17-297-2017

Gutleben, M., Groß, S., Wirth, M., & Mayer, B. (2020). Radiative effects of long-range-transported Saharan air layers as determined from airborne lidar measurements. *Atmospheric Chemistry and Physics*, *20*, 12313–12327. https://doi.org/10.5194/acp-20-12313-2020

Gutleben, M., Gross, S., Wirth, M., Emde, C., & Mayer, B. (2019). Impacts of water vapor on Saharan air layer radiative heating. *Geophysical Research Letters*, *46*(24), 14854–14862. https://doi.org/10.1029/2019gl085344

Hess, M., Koepke, P., & Schult, I. (1998). Optical properties of aerosols and clouds: The software package OPAC. *Bulletin of the American Meteorological Society*, *79*(5), 831–844. https://doi.org/10.1175/1520-0477(1998)079<0831:Opoaac>2.0.Co

Ismail, S., Ferrare, R. A., Browell, E. V., Kooi, S. A., Dunion, J. P., Heymsfield, G., et al. (2010). LASE measurements of water vapor, aerosol, and cloud distributions in Saharan air layers and tropical disturbances. *Journal of the Atmospheric Sciences*, *67*(4), 1026–1047. https://doi.org/10.1175/2009jas3136.1

Kanitz, T., Engelmann, R., Heinold, B., Baars, H., Skupin, A., & Ansmann, A. (2014). Tracking the Saharan air layer with shipborne lidar across the tropical Atlantic. *Geophysical Research Letters*, *41*(3), 1044–1050. https://doi.org/10.1002/2013gl058780

Karyampudi, V. M., Palm, S. P., Reagen, J. A., Fang, H., Grant, W. B., Hoff, R. M., et al. (1999). Validation of the Saharan dust plume conceptual model using lidar, Meteosat, and ECMWF data. *Bulletin of the American Meteorological Society*, *80*(6), 1045–1075. https://doi.org/10.1175/1520-0477(1999)080<1045:votsdp>2.0.co;2

Kealy, J. C., Marenco, F., Marsham, J. H., Garcia-Carreras, L., Francis, P. N., Cooke, M. C., & Hocking, J. (2017). Clouds over the summertime Sahara: An evaluation of Met Office retrievals from Meteosat Second Generation using airborne remote sensing. *Atmospheric Chemistry and Physics*, *17*(9), 5789–5807. https://doi.org/10.5194/acp-17-5789-2017

Korolev, A. V., Strapp, J. W., Isaac, G. A., & Nevzorov, A. N. (1998). The Nevzorov airborne hot-wire LWC-TWC probe: Principle of operation and performance characteristics. *Journal of Atmospheric and Oceanic Technology*, *15*(6), 1495–1510. https://doi.org/10.1175/1520-0426(1998)015<1495:Tnahwl>2.0.Co

Liu, D. T., Taylor, J., Crosier, J., Marsden, N., Bower, K. N., Lloyd, G., et al. (2018). Aircraft and ground measurements of dust aerosols over the west African coast in summer 2015 during ICE-D and AER-D. *Atmospheric Chemistry and Physics*, *18*(5), 3817–3838. https://doi.org/10.5194/acp-18-3817-2018

Liu, Z. Y., Omar, A., Vaughan, M., Hair, J., Kittaka, C., Hu, Y. X., et al. (2008). CALIPSO lidar observations of the optical properties of Saharan dust: A case study of long-range transport. *Journal of Geophysical Research-Atmospheres*, *113*(D7), D07207. https://doi.org/10.1029/2007jd008878

Mallios, S. A., Drakaki, E., & Amiridis, V. (2020). Effects of dust particle sphericity and orientation on their gravitational settling in the Earth's atmosphere. *Journal of Aerosol Science*, *150*, 105634. https://doi.org/10.1016/j.jaerosci.2020.105634

Manners, J., Edwards, J., Hill, P., & Thelen, J.-C. (2017). *SOCRATES technical guide suite of community radiative transfer codes based on Edwards and Slingo*.

Mantsis, D. F., Sherwood, S., Dixit, V., Morrison, H., & Thompson, G. (2020). Mid-level clouds over the Sahara in a convection-permitting regional model. *Climate Dynamics*, *54*(7–8), 3425–3439. https://doi.org/10.1007/s00382-020-05188-4

Marenco, F., Ryder, C., Estelles, V., O'Sullivan, D., Brooke, J., Orgill, L., et al. (2018). Unexpected vertical structure of the Saharan Air Layer and giant dust particles during AER-D. *Atmospheric Chemistry and Physics*, *18*(23), 17655–17668. https://doi.org/10.5194/acp-18-17655-2018

Marsham, J. H., Hobby, M., Allen, C. J. T., Banks, J. R., Bart, M., Brooks, B. J., et al. (2013). Meteorology and dust in the central Sahara: Observations from Fennec supersite-1 during the June 2011 Intensive Observation Period. *Journal of Geophysical Research: Atmospheres*, *118*(10), 4069–4089. https://doi.org/10.1002/jgrd.50211

Marsham, J. H., Parker, D. J., Grams, C. M., Taylor, C. M., & Haywood, J. M. (2008). Uplift of Saharan dust south of the intertropical discontinuity. *Journal of Geophysical Research: Atmospheres*, *113*(D21), D21102. https://doi.org/10.1029/2008jd009844

Marsham, J. H., Parker, D. J., Todd, M. C., Banks, J. R., Brindley, H. E., Garcia-Carreras, L., et al. (2016). The contrasting roles of water and dust in controlling daily variations in radiative heating of the summertime Saharan heat low. *Atmospheric Chemistry and Physics*, *16*(5), 3563–3575. https://doi.org/10.5194/acp-16-3563-2016

Marsham, J. H., & Ryder, C. L. (2021). Weather Insight—Dust storms and haboobs. *Weather*. WEA4071. https://doi.org/10.1002/wea.4071

O'Sullivan, D., Marenco, F., Ryder, C. L., Pradhan, Y., Kipling, Z., Johnson, B., et al. (2020). Models transport Saharan dust too low in the atmosphere: A comparison of the MetUM and CAMS forecasts with observations. *Atmospheric Chemistry and Physics*, *20*(21), 12955–12982. https://doi.org/10.5194/acp-20-12955-2020

Pistone, K., Zuidema, P., Wood, R., Diamond, M., da Silva, A. M., Ferrada, G., et al. (2021). Exploring the elevated water vapor signal associated with the free-tropospheric biomass burning plume over the southeast Atlantic Ocean. *Atmospheric Chemistry and Physics*, *21*, 9643–9668. https://doi.org/10.5194/acp-21-9643-2021

Prospero, J. M., & Carlson, T. N. (1972). Vertical and areal distribution of Saharan dust over Western Equatorial North-Atlantic Ocean. *Journal of Geophysical Research*, *77*(27), 5255–5265. https://doi.org/10.1029/JC077i027p05255

Randles, C., Kinne, S., Myhre, G., Schulz, M., Stier, P., Fischer, J., et al. (2012). Intercomparison of shortwave radiative transfer schemes in global aerosol modeling: Results from the AeroCom Radiative Transfer Experiment. *Atmospheric Chemistry and Physics Discussions*, *12*(12), 32631–32706. https://doi.org/10.5194/acpd-12-32631-2012

Roberts, A. J., Marsham, J. H., Knippertz, P., Parker, D. J., Bart, M., Garcia-Carreras, L., et al. (2017). New Saharan wind observations reveal substantial biases in analysed dust-generating winds. *Atmospheric Science Letters*, *18*(9), 366–372. https://doi.org/10.1002/asl.765

Rothman, L. S., Barbe, A., Benner, D. C., Brown, L. R., Camy-Peyret, C., Carleer, M. R., et al. (2003). The HITRAN molecular spectroscopic database: Edition of 2000 including updates through 2001. *Journal of Quantitative Spectroscopy & Radiative Transfer*, *82*(1–4), 5–44. https://doi.org/10.1016/S0022-4073(03)00146-8

Ryder, C. L., Highwood, E. J., Walser, A., Seibert, P., Philipp, A., & Weinzierl, B. (2019). Coarse and giant particles are ubiquitous in Saharan dust export regions and are radiatively significant over the Sahara. *Atmospheric Chemistry and Physics*, *19*(24), 15353–15376. https://doi.org/10.5194/acp-19-15353-2019

Ryder, C. L., Marenco, F., Brooke, J. K., Estelles, V., Cotton, R., Formenti, P., et al. (2018). Coarse-mode mineral dust size distributions, composition and optical properties from AER-D aircraft measurements over the tropical eastern Atlantic. *Atmospheric Chemistry and Physics*, *18*(23), 17225–17257. https://doi.org/10.5194/acp-18-17225-2018

Tsamalis, C., Chedin, A., Pelon, J., & Capelle, V. (2013). The seasonal vertical distribution of the Saharan Air Layer and its modulation by the wind. *Atmospheric Chemistry and Physics*, *13*(22), 11235–11257. https://doi.org/10.5194/acp-13-11235-2013

van der Does, M., Knippertz, P., Zschenderlein, P., Harrison, R. G., & Stuut, J. B. W. (2018). The mysterious long-range transport of giant mineral dust particles. *Science Advances*, *4*(12), eaau2768. https://doi.org/10.1126/sciadv.aau2768

Volz, F. E. (1973). Infrared optical-constants of ammonium sulfate, Sahara dust, volcanic pumice, and flyash. *Applied Optics*, *12*(3), 564–568. https://doi.org/10.1364/Ao.12.000564

Walters, D. N., Best, M. J., Bushell, A. C., Copsey, D., Edwards, J. M., Falloon, P. D., et al. (2011). The Met Office Unified Model Global Atmosphere 3.0/3.1 and JULES Global Land 3.0/3.1 configurations. *Geoscientific Model Development*, *4*(4), 919–941. https://doi.org/10.5194/gmd-4-919-2011

Weinzierl, B., Ansmann, A., Prospero, J. M., Althausen, D., Benker, N., Chouza, F., et al. (2017). The Saharan aerosol long-range transport and aerosol-cloud-interaction experiment: Overview and selected highlights. *Bulletin of the American Meteorological Society*, *98*(7), 1427–1451. https://doi.org/10.1175/Bams-D-15-00142.1

Wong, S., & Dessler, A. E. (2005). Suppression of deep convection over the tropical North Atlantic by the Saharan Air Layer. *Geophysical Research Letters*, *32*(9). https://doi.org/10.1029/2004gl022295

Wong, S., Dessler, A. E., Mahowald, N. M., Yang, P., & Feng, Q. (2009). Maintenance of lower tropospheric temperature inversion in the Saharan air layer by dust and dry anomaly. *Journal of Climate*, *22*(19), 5149–5162. https://doi.org/10.1175/2009jcli2847.1

Yu, H., Tan, Q., Zhou, L., Bian, H. S., Chin, M., Ryder, C. L., et al. (2021). Observation and modeling of a gigantic African dust intrusion into the Caribbean Basin and the southern U.S. in June 2020. *Atmospheric Chemistry and Physics*, *21*, 12359–12383. https://doi.org/10.5194/acp-21-12359-2021

Zdunkowski, W. G., Welch, R. M., & Korb, G. (1980). An investigation of the structure of typical two-stream methods for the calculation of solar fluxes and heating rates in clouds. *Beitrage zur Physik der Atmosphare*, *53*, 147–166.